Journal of Structural Biology 218 (2026) 108282

Contents lists available at ScienceDirect

Journal of Structural Biology

journal homepage: www.elsevier.com/locate/yjsbi

Research Article

Probing the structure and thermodynamics of a multidomain psychrophilic chitinase from *Moritella marina*

Magdalena Bejger [1], Piotr H. Małecki [1], Katarzyna Biniek-Antosiak, Wojciech Rypniewski [*]

Institute of Bioorganic Chemistry, Polish Academy of Sciences, ul. Noskowskiego 12/14, 61-704 Poznań, Poland

ARTICLE INFO

Editor: Bauke Dijkstra

Keywords:
Chitinase
Moritella marina
Protein structure
Crystallography
Psychrophile

ABSTRACT

Studies of protein structure and stability have traditionally focused on individual domains, treating them as autonomous units, even though most proteins consist of multiple domains. This raises the question to what extent can multidomain proteins be considered as sums of their individual domains, and how neighboring domains influence one another. Chitinase Chi60 from the psychrophilic bacterium *Moritella marina* consists of four domains linked in sequence: a catalytic domain, two consecutive Ig-like domains, and a chitin-binding module. The modular architecture of this enzyme provides an opportunity to examine the structure and stability of a protein from which domains are systematically excised. A series of deletion mutants of the chitinase was designed and constructed, and their structures and thermal melting profiles were analyzed. The different domains exhibit distinct melting temperatures. The catalytic domain shows a complex melting profile. Each domain can fold and maintain its structural integrity when isolated, including the two tandem Ig-like domains that share sequence similarity. Although the interfaces between domains in this modular protein are small, it is still possible to detect the influence neighboring domains exert on one another. Some artificial combinations of domains are unstable and prone to degradation. This long, flexible molecule may be stabilized through dimerization when not engaged with the chitin substrate, with two of its domains participating in the interaction.

1. Introduction

Most proteins contain more than one domain; many consist of several domains. Each domain may confer a specific property on the protein, allowing it to combine different properties and functions. Studies of protein structure, function and stability have primarily focused on individual domains, treating them as autonomous units and grouping them into taxonomic families. This approach is justified because similar domains usually share a common evolutionary origin and retain their characteristics even when incorporated into a larger assembly. However, this perspective has limitations, as domains significantly influence one another, e.g. in terms of stability (Han et al., 2007).

Natural multidomain proteins are optimized products of evolution, whereas laboratory constructs often fail to produce stable proteins. The mutual arrangement of domains may be crucial for protein function, yet it remains difficult to predict even when individual domains can be modeled with increasing accuracy using modern AI tools. Experimental studies of multidomain proteins are often challenging because these proteins tend to be flexible, making them difficult to capture in structural analysis. As a result, structures of multidomain proteins are frequently solved in parts rather than as complete assemblies.

Many chitinases have a multidomain organization. In addition to the catalytic domain, they may contain auxiliary domains that enhance enzymatic efficiency and increase the enzyme's affinity for chitin. Chitin, a polymer of *N*-acetyl-D-glucosamine (GlcNAc) units linked by β-(1 → 4) covalent bonds, forms a dense network of interchain hydrogen bonds that render it insoluble in water and highly resistant to degradation.

Chitinase 60 (EC 3.2.1.14) from the psychrophilic bacterium *Moritella marina* (*Mm*Chi60) is a 60 kDa enzyme belonging to glycoside hydrolase family 18 (GH18). It comprises four domains: a catalytic $(\beta\alpha)_8$ TIM-barrel domain (CAT), two consecutive immunoglobulin-like (Ig-

Abbreviations: CAT, the catalytic $(\beta\alpha)_8$ TIM-barrel domain; Ig1 & Ig2, Ig-like domains number 1 and number 2; CBM, chitin-binding module or domain; GlcNAc, *N*-acetyl-D-glucosamine; DSC, differential scanning calorimetry; cryo-EM, cryogenic electron microscopy; DLS, dynamic light scattering; MPD, 2-methyl-2,4-pentanediol; MES, 2-(*N*-morpholino)ethanosulfonic acid.

* Corresponding author.
E-mail address: wojtekr@ibch.poznan.pl (W. Rypniewski).

[1] These authors contributed equally to this work.

https://doi.org/10.1016/j.jsb.2025.108282
Received 7 November 2025; Received in revised form 16 December 2025; Accepted 18 December 2025
Available online 26 December 2025

like) domains (Ig1 and Ig2), and a chitin-binding module (CBM) (Malecki et al., 2013). X-ray crystallography revealed that the protein is highly elongated, approximately 125 Å in length, with domains arranged in a linear chain and evidence of flexibility between them (Malecki et al., 2014).

The active site is located at the carboxyl ends of the β-barrel, similar to other enzymes with the TIM-barrel architecture, and features a relatively shallow substrate-binding groove compared to other chitinases. This has been interpreted as a mechanism to maximize substrate accessibility and facilitate catalysis at the low working temperatures characteristic of this cold-adapted enzyme (Malecki et al., 2013). The substrate-binding groove was characterized in a ligand-binding crystallographic study of a low-activity *Mm*Chi60 mutant (Malecki et al., 2014), for five consecutive GlcNAc residues in subsites numbered –2, –1, +1, +2 and +3, according to the Henrissat nomenclature system (Davies et al., 1997). The scissile bond is the glycosidic bond located between the sugar units in subsites –1 and +1. On the + (aglycon) side, the substrate-binding site extends toward a β-hairpin (strands 6a–6b, Fig. 1) on the protein's surface, forming a tongue-like structure with a tryptophan patch (Trp234, Trp228). The hairpin exhibits some mobility and has been proposed to function as a secondary chitin-binding element, facilitating the orientation and dislodgement of a $(GlcNAc)_n$ chain from the bulk chitin before hydrolysis (Malecki et al., 2014).

The immunoglobulin (Ig) fold is typically associated with the vertebrate immune system, but immunoglobulin-like (Ig-like) domains—known as Big 3 domains (Pfam database ID PF07523)— share structural and amino acid sequence similarities with canonical Ig domains and are found in diverse proteins across a wide range of

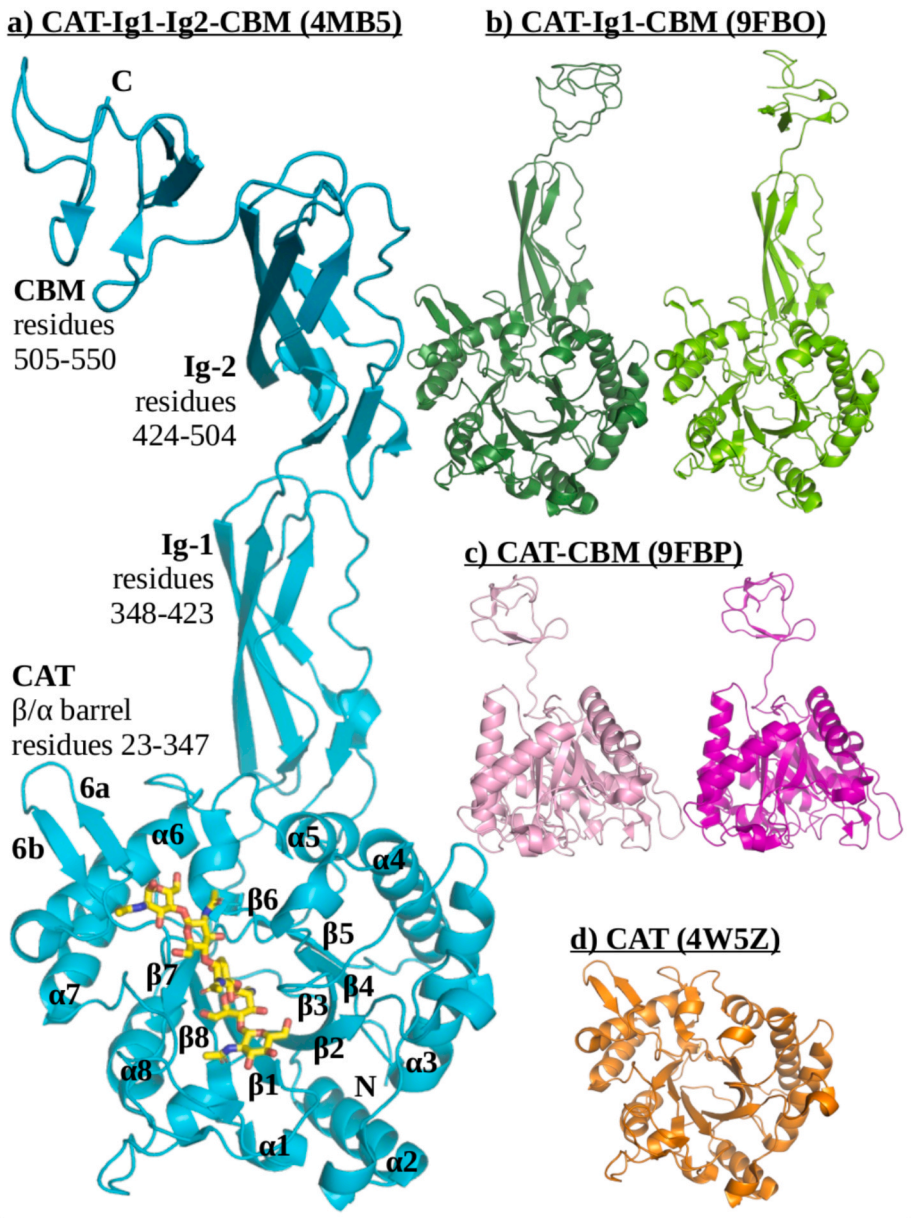

Fig. 1. Overview of the crystal structures of *Mm*Chi60 deletion mutants. (a) Structure of the low activity mutant (E153Q) of the enzyme, consisting of catalytic (CAT), two Ig-like (Ig-1, Ig-2), and the chitin-binding (CBM) domains is shown in cyan (Malecki et al., 2014). The secondary structure elements of the CAT $(\beta\alpha)_8$ domain and the 6a–6b β-hairpin are labeled; the N- and C-termini are indicated. Bound $(GlcNAc)_5$ is shown (yellow sticks), marking the substrate-binding groove, subsites –2 to +3, from bottom up. (b) Two crystallographically independent molecules of the CAT–Ig1–CBM mutant (light and dark green), (c) two independent molecules of the CAT–CBM mutant (light and dark pink) and (d) the structure of the CAT deletion mutant (orange) are shown. The CAT–CBM structures are shown in a different orientation from the other structures, so that the CBM domains can be seen.

organisms. These domains are often involved in cell adhesion or cell surface receptor functions (Barclay, 1999). Ig-like domains are also present in chitinases, where they have been proposed to enhance flexibility or stabilize these multidomain proteins (Itoh et al., 2016; Malecki et al., 2013).

The chitin binding module (CBM) of *Mm*Chi60 belongs to Carbohydrate-Binding Module Family 5/12 (Pfam database ID PF02839). CBMs in this family are small (45–60 amino acid residues) accessory domains found in many glycosyl hydrolases, including chitinases and endoglucanases. They enhance the protein's affinity for chitin and are characterized by surface-exposed aromatic residues that likely contribute to binding chitin (Ikegami et al., 2000). In *Mm*Chi60, the CBM contains three co-planar Trp residues on its surface (Trp533, Trp534, and Trp546) (Malecki et al., 2013).

Recent studies of deletion mutants of multidomain chitinases include the enzymatic and thermodynamic characterization of a three-domain chitinase C from *Serratia marcescens*, consisting of catalytic, fibronectin type III (structurally related to Ig-like) and chitin-binding domains. Removal of the accessory domains had a moderate effect—observed by CD spectroscopy—on the catalytic activity and structural integrity of the remaining parts of the molecule (Lin et al., 2015). Crystal structures of two truncated mutants of a multidomain bacterial chitinase, ChiW, which possesses two catalytic domains, were also analyzed: (1) ChiW lacking the SLH domains that anchor the enzyme to the cell wall, and (2) ChiW with an additional removal of a chitin-binding module (CBM-54) and one of its two Ig-like domains (Itoh et al., 2016). The authors reported that the Ig-like domains were bound to the catalytic domains and might function to stabilize them, while the CBM-54 domain interacted with cell wall polysaccharides, which could enable the enzyme to dock to the target cell wall. A study of ChiB and ChiC chitinases from *Serratia marcescens* showed that the CBM domains support the catalytic efficiency of these enzymes and that their removal makes the chitinases more sensitive to heat deactivation (Liu et al., 2023).

A study of another thermostable protein, superoxide dismutase, revealed an interesting effect of a protein domain whose presence conferred heat resistance on the protein to which it was attached (Wang et al., 2014). Deleting this domain reduced the thermostability of the enzyme, while attaching the domain to a mesophilic enzyme enhanced its thermostability.

The modular structure of *Mm*Chi60 presents an attractive model for investigating the structure and thermodynamics of multidomain proteins. The native protein was amenable to crystallographic analysis, and preliminary thermal melting profiles have revealed distinct peaks that can be attributed to its individual domains (Stavros et al., 2015). Here, we present an extended study of the structure and thermodynamic stability of *Mm*Chi60 deletion mutants.

2. Results

2.1. Design of MmChi60 mutants

Deletion mutants were designed to investigate the effect of individual domains on the protein's structure and stability (Fig. 1). The crystal structure of native *Mm*Chi60 was first examined to identify hinge regions between domains where separation could occur without destabilizing the protein (Table 1). All mutants were constructed solely through deletions in the native amino acid sequence—no artificial linkers were introduced. The design process was guided by previous findings reported by (Stavros et al., 2015). Although the protein domains appear clearly distinguishable from one another, the subsequent task of disassembling them proved challenging in some cases.

Initially, mutants were generated in which each of the two Ig-like domains was excised (CAT–Ig1–CBM, CAT–Ig2–CBM). The deleted residue ranges were 423–504 and 348–423, respectively. Both proteins were successfully purified, but only CAT–Ig1–CBM produced crystals of an intact mutant, for which the structure was solved (PDB ID: 9FBO). CAT–Ig2–CBM was prone to degradation and yielded crystals containing only the CAT domain.

Three mutants lacking both Ig-like domains were prepared (CAT–CBM-5, CAT–CBM-8 and CAT–CBM-2). CAT–CBM-5 had the same construction as described by (Stavros et al., 2015), with residues 348–504 excised. Crystallization of CAT–CBM-5 produced crystals under various conditions, however, all the initially solved structures contained only the CAT domain (PDB IDs: 4W5Z, 9FBR, 9FBS). Subsequently, mutants were constructed with either a longer linker (CAT–CBM-8, residues 348–501 excised) or a shorter one (CAT–CBM-2, residues 346–505 excised).

The stability of the three CAT–CBM variants was assessed by incubating the proteins at 4 °C for approximately three months (Fig. S1). CAT–CBM-8 showed the fastest degradation, whereas CAT–CBM-2 was the most stable. Eventually, conditions were identified for relatively rapid crystallization of CAT–CBM-5, yielding crystals containing both protein domains (PDB ID: 9FBP).

A mutant consisting solely of the catalytic domain (CAT; residues 23–345) was also constructed, and its structure was solved (PDB ID: 9FBQ). In addition, a mutant comprising only the Ig-like domains (Ig1–Ig2; residues 348–506) and another containing only the chitin-binding module (CBM; residues 507–550) were generated. Both were successfully expressed and purified, but no crystals were obtained.

Regardless of their crystallizability, all purified mutants were subjected to thermodynamic analyses.

2.2. Structure of the catalytic domain (CAT) of MmChi60

Four crystal structures of isolated catalytic domains were determined in this study. Crystals were obtained for the CAT deletion mutant (PDB ID: 9FBQ). In addition, three crystallization attempts of CAT–CBM-5 mutants yielded crystals that contained only the catalytic domain (PDB

Table 1
Summary of *Mm*Chi60 mutants.

***Mm*Chi60 and its deletion mutants**	**Amino acid residue numbers, MW**				**PDB ID**
	CAT domain	**Ig-like-1 domain**	**Ig-like-2 domain**	**CBM domain**	
CAT–Ig1–Ig2–CBM 59 kDa (native form)	23–347 36 kDa	348–423 8 kDa	424–504 8 kDa	505–550 5 kDa	4HMC (Malecki et al., 2013)
CAT–Ig1–CBM 50 kDa	23–347 36 kDa	348–422 8 kDa		505–550 5 kDa	9FBO
CAT–Ig2–CBM 50 kDa	23–347 36 kDa		424–504 8 kDa	505–550 5 kDa	Only CAT in crystals, not deposited
CAT–CBM-5 42 kDa	23–347 36 kDa			505–550 5 kDa	9FBP
					4W5Z, 9FBR, 9FBS (only CAT found)
CAT–CBM-8 42 kDa	23–347 36 kDa			502–550 5 kDa	Only CAT in crystals, not deposited
CAT–CBM-2 42 kDa	23–345 36 kDa			506–550 5 kDa	Only CAT in crystals, not deposited
CAT 36 kDa	23–345 36 kDa				9FBQ
Ig1–Ig2 18 kDa		348–423 8 kDa	424–506 8 kDa		No crystals
CBM 5 kDa				507–550 5 kDa	No crystals

IDs: 4W5Z, 9FBR, 9FBS) (Table 1). The CBM domain was apparently cleaved off by an unidentified degradation process. All crystals belonged to space group $C222_1$ and exhibited nearly identical unit cell parameters, despite being grown under different crystallization conditions (see *Materials and Methods*). When the four CAT structures are superposed pairwise, the root-mean-square differences between the C_α atoms in each pair range between 0.22 and 0.33 Å. The structure with the highest resolution (1.32 Å; PDB ID: 4W5Z) was used for subsequent analysis and comparisons.

Interactions between CAT domains in the crystal lattice showed no correspondence to the "dimerization" interactions observed in the native *Mm*Chi60 structure or in the CAT–Ig1–CBM mutant (see below), both of which dimerize within the crystal lattice.

The structure of the isolated CAT domain is highly similar to that of the CAT domain within native *Mm*Chi60 (PDB ID: 4HMC). Even the C-terminal tail of CAT (Gln341–Leu342–Pro343–Pro344–Val345, following helix α8) remains well ordered and retains the same conformation as in the native protein. Most of the ordered water molecules within the cavity between the tail and the bulk of the CAT domain are also conserved (Fig. 2C).

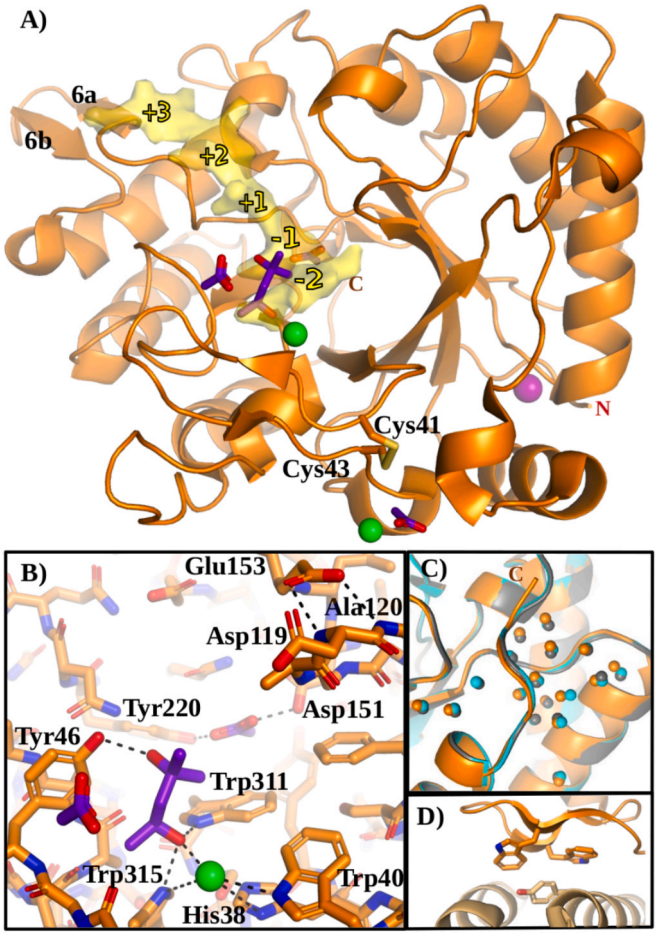

Fig. 2. Structure of the CAT domain (PDB ID: 4W5Z). A) The substrate-binding subsites, identified earlier (Malecki et al., 2014), from –2 to +3, have been marked, as well as the 6a–6b β-hairpin (see the main text for explanation), the Cys41–Cys43 disulfide bridge, MPD and acetate anions (*violet* sticks with *red* O atoms) bound in the substrate-binding groove, chloride ions (*green* balls), sodium ion (*pink* ball). B) Details of the small ligands binding in the substrate-binding site. C) The C-terminal tail of the deletion mutant (*orange*) maintains its stability and conformation compared to the native enzyme (cyan). Most water molecules in an adjacent cavity are also conserved. D) The 6a–6b β-hairpin interacts, via Trp234 and Trp228, with the neighboring protein molecule in the crystal lattice (see the main text for explanation).

Further similarities between the isolated CAT and the catalytic domain in native *Mm*Chi60 are revealed upon detailed comparison. These include a Cys41–Cys53 disulfide bridge and a sodium cation coordinated by the side chains of Asn105 and Asp146, along with the carbonyl oxygen atoms of Gly144 and Thr24. Small ligands from the crystallization medium were found bound in the substrate-binding groove: a 2-methyl-2,4-pentanediol (MPD) molecule and an acetate ion (Figs. 2A and 2B). The MPD molecule spans subsites –2 to +1, corresponding to those observed in the structure of the low-activity *Mm*Chi60 mutant complexed with $(GlcNAc)_5$ (Malecki et al., 2014). One hydroxyl group of MPD occupies the position of the acetyl group of the GlcNAc residue in the –2 subsite, interacting with the Nε1 atoms of Trp311 and Trp315. The other hydroxyl group occupies the position of the acetyl group of GlcNAc in the +1 subsite and forms a hydrogen bond with Tyr46. The acetate molecule interacts with the oxygen atom of Asp151 and the hydroxyl group of Tyr220, like the acetyl group of the GlcNAc residue in the –1 subsite. Additionally, two chloride anions and two more acetate ions were modeled on the protein surface.

The active-site residue Glu153 (the acid/base in the catalytic reaction) is "parked" against the main-chain NH groups of Asp119 and Ala120 on a flexible loop, as previously observed in the unliganded *Mm*Chi60 structure. This conformation has been proposed to represent the enzyme's resting state in the absence of substrate (Malecki et al., 2013).

The main structural difference between the present CAT structure and the catalytic domain of unliganded *Mm*Chi60 lies in the position of the 6a–6b β-hairpin (residues 226–236) on the aglycon side of the substrate-binding site. The β-hairpin is shifted by up to 3 Å relative to the unliganded native structure. It participates, *via* stacking interactions, in intermolecular contacts within the crystal lattice (Fig. 2D). The mobility of the 6a–6b β-hairpin had been noted previously and discussed in relation to the enzyme's affinity for chitin. It has been hypothesized to function as a structural element that loosens a strand of poly-GlcNAc from the crystalline chitin matrix, thereby priming it for hydrolysis.

2.3. Structure of the CAT–CBM deletion mutant of MmChi60

The unit cell was right-angled, initially suggesting an orthorhombic lattice, however, the crystal was ultimately determined to be monoclinic, belonging to space group $P2_1$, and twinned (the twinning fraction refined to 0.54). The asymmetric unit contained two crystallographically independent CAT–CBM-5 molecules related by a noncrystallographic twofold axis (Fig. 3). Crystal twinning arises from alternative conformations of CAT–CBM-5 molecules, in which the CAT and CBM domains adopt different relative orientations (Fig. 3, inset). The shift between domains pivots around Asp347—the terminal residue of the CAT domain—and results in displacements of up to 4.7 Å in the CBM domain.

Despite conformational differences between the CAT–CBM-5 molecules, most of the their intermolecular contacts are similar, particularly those involving the CBM domains. The Trp533 and Trp534 residues of the CBM domains interact with the CAT domains of neighboring molecules (Fig. S2). Interactions between CAT domains in the CAT–CBM-5 structure differ from the "dimerization" interactions observed in the native *Mm*Chi60 structures and in the CAT–Ig1–CBM mutant (see below).

The overall folds of both the CAT and CBM domains are preserved relative to those in native *Mm*Chi60. Minor variations in secondary structure elements can be attributed to packing effects or uncertainties in atomic positioning related to X-ray resolution. Structural similarities with native *Mm*Chi60 and other mutant forms extend to notable details, including the Cys41–Cys43 disulfide bridge and the presence of a sodium ion in the CAT domain (see above). The active-site residue Glu153 remains in the "parked" conformation, which has been proposed to represent the enzyme's resting state.

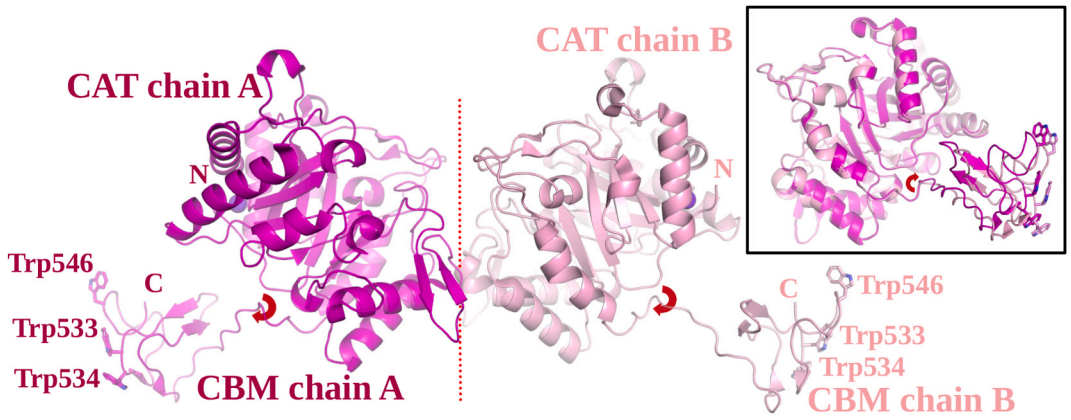

Fig. 3. The two crystallographically independent CAT–CBM-5 mutant molecules in the asymmetric unit (shown in dark and light *pink*). The noncrystallographic twofold symmetry axis is marked with a *red* dotted line. Structures of the CAT domains are very similar, but the CBM domains differ in position by approx. 4 Å (see inset). The flexible regions enabling the shift are indicated by *red* arrows. The three characteristic Trp residues on the surface of CBM domains are shown and labeled (see text for discussion and Fig. S2 for details).

2.4. Structure of the CAT–Ig1–CBM deletion mutant of MmChi60

In the crystal lattice two CAT–Ig1–CBM molecules are present in the asymmetric unit (Fig. 4). Considerable disorder is observed in the crystal structure, particularly in chain B, which is more solvent-exposed than chain A. This disorder is likely related to the relatively low resolution (2.69 Å) of the X-ray diffraction data and the higher than average solvent content in the crystal lattice (62 %).

CAT–Ig1–CBM molecules form "dimers" exhibiting noncrystallographic twofold symmetry. These dimers can be compared to the crystallographic dimers formed by the native *Mm*Chi60 molecules (Malecki et al., 2013) (Figs. 4 and 5). Interactions between the CAT domains in the mutant and in the native *Mm*Chi60 structures are similar. They involve the loops between β5 and α5 (residues 188–202), between α6 and β7 (residues 256–269), and the β-hairpin 6a–6b (residues 226–236) (Fig. 5A).

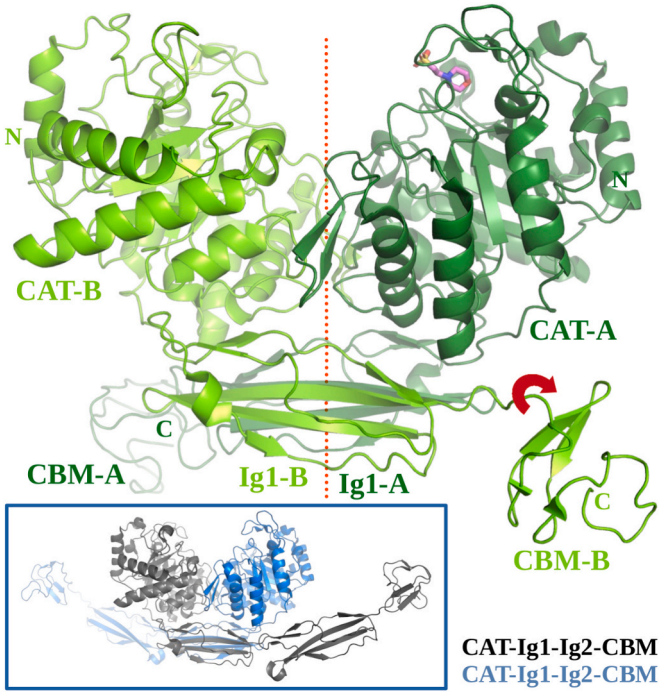

Fig. 4. The two CAT–Ig1–CBM mutant molecules in the asymmetric unit (chains A and B shown in dark and light *green*) interact similarly to the native *Mm*Chi60 structure, shown in the inset (Malecki et al., 2013) (PDB ID: 4HMC). The N- and C-termini are indicated. The MES molecule, bound in the substrate-binding site, is drawn as sticks. The noncrystallographic twofold symmetry axis is shown as a *red* dotted line. The hinge region, responsible for the flexibility of the CBM domain is indicated by a curved arrow (*red*).

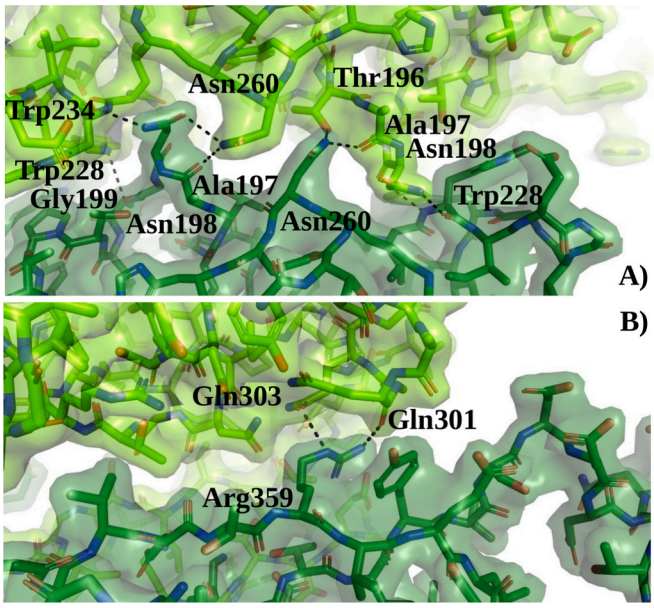

Fig. 5. Hydrogen-bonding interactions (dotted lines) between (**A**) the CAT domains and (**B**) the CAT and Ig1 domains in the CAT–Ig1–CBM mutant structure. The interactions are similar to those observed in the native structure of *Mm*Chi60 (PDB ID: 4HMC) and are probably responsible for dimerization of the molecules in the crystal lattice and in cryo-EM studies (see the main text).

Intermolecular interactions between the CAT and Ig1 domains in the mutant are also conserved relative to the native structure (Fig. 5B). These include hydrogen-binding and stacking interactions between Gln301 and Gln303 of the CAT domain and Arg359 of the Ig1 domain. Additionally, interactions occur between the Ig1 domains themselves: Asn414 of one Ig1 domain forms hydrogen bonds with Asp399 and Lys418 of the other Ig1 domain, and *vice versa*. These contacts are absent in the crystals structure of the native protein, due to a relative shift of approximately 4 Å between the Ig1 domains.

The CBM domains of each CAT–Ig1–CBM dimer form similar contacts with neighboring protein molecules, even though the neighboring molecules are oriented 120° relative to each other (due to the

crystallographic threefold axis), whereas the two CAT–Ig1–CBM molecules in the asymmetric unit are rotated by approximately 180° with respect to each other (due to the noncrystallographic twofold axis) (Fig. S3). Matching interactions between CAT–Ig1–CBM dimers and their symmetry-related neighbors are possible because of the flexibility of the CBM domains relative to the rest of the molecule.

Superposition of the C_α atoms of the two protein molecules (chains A and B) revealed that while the CBM, CAT and Ig1 domains each retain their respective folds, the CBM domains differ by a rotation of approximately 140° about the long axis of the molecule. This flexibility arises from a short hinge region comprising residues Ser506–Asp507–Asp508–Asp509 at the beginning of the CBM sequence.

In one of the molecules (chain A), additional electron density was observed in the substrate-binding groove and was interpreted as a 2-(*N*-morpholino)ethanesulfonic acid (MES) molecule, which was present in the crystallization medium. The ligand interacts with Trp residues (Trp40, Trp311 and Trp315) that line the bottom of the substrate-binding groove at the –1 and –2 subsites. The catalytic residue Glu153 remains in the "parked" conformation, positioned against the main-chain NH groups of Asp119 and Ala120, as observed in the other structures.

2.5. Cryogenic electron microscopy (cryo-EM)

Preliminary analysis of the cryo-EM data, performed through multiple rounds of 2D classification, revealed a heterogeneous particle population. Most of the 2D class averages displayed dimeric assemblies of *Mm*Chi60, in which only the CAT domain was clearly discernible. A smaller subset of particles, corresponding in size to monomers, was also observed (Fig. 6).

The overall architecture of the dimer is consistent with previously reported crystal structures. The dimensions observed in the 2D classes align well with the expected span of two catalytic domains interacting to form a dimer. Moreover, several classes displayed distinct features forming visible bridges that connect the two globular domains. At this stage of analysis, some of the higher-quality 2D classes revealed fine structural details, including features suggestive of secondary structural elements.

2.6. Thermal stability and melting profiles of MmChi60 and its mutants

Microcalorimetric measurements of *Mm*Chi60 and its mutants revealed detailed thermostability profiles that can be interpreted in terms of the stability of individual protein domains, both in isolation and in relation to neighboring domains (Figs. 7 and 8).

The CAT domain is the most stable, with an overall T_m of approximately 55 °C. Its melting profile is asymmetric, indicating that unfolding of this domain is not a simple one-step process (Fig. 8e). The melting behavior can be interpreted as two thermal events, with peaks at 51 °C and 54 °C for CAT when connected to other domains, and at 53 °C and

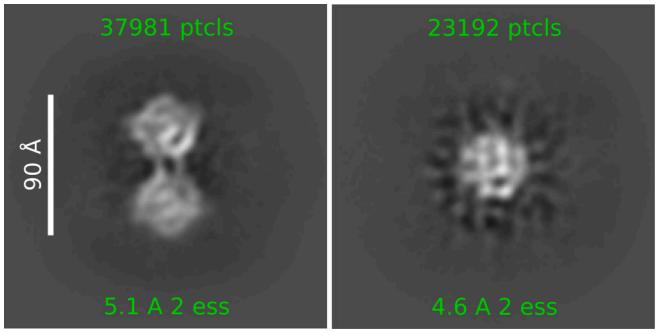

Fig. 6. Cryo-EM 2D classes representing a dimeric and a monomeric form of *Mm*Chi60. Only the CAT domain is visible.

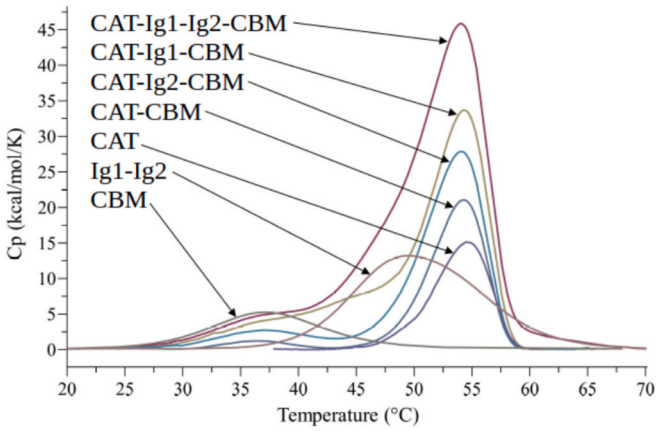

Fig. 7. Superposition of DSC melting profiles of the native *Mm*Chi60 (CAT–Ig1–Ig2–CBM) and the deletion mutants analyzed in this work.

55 °C for the isolated CAT domain.

The CBM domain is the least stable, with a T_m of 38–39 °C, when it forms part of the native *Mm*Chi60 or the CAT–Ig1/Ig2–CBM mutants (Fig. 8abc). It is slightly less stable (T_m = 37 °C) in the CAT–CBM mutant (Fig. 8d), where it is directly adjacent to the CAT domain without intervening Ig-like domain(s). The CBM appears to retain its structural integrity when expressed independently, showing a T_m of 37 °C (Fig. 8g).

The Ig-like domains exhibit intermediate thermal stability, between that of CAT and CBM, with T_m values of 47–49 °C in the native *Mm*Chi60 protein or when present in the CAT–Ig1/Ig2–CBM mutants (Fig. 8abc). Their melting profile is partially obscured by its proximity to the dominant CAT domain peak. When the Ig1–Ig2 domains are expressed alone, they appear to maintain structural integrity, displaying a single peak with a T_m of approximately 50 °C (Fig. 8f).

3. Discussion

Studies of protein structure and stability have traditionally focused on individual domains treated as autonomous units, even though most proteins contain more than one domain. Viewing multidomain proteins as simple sums of their individual domains is an oversimplification, while studying them in their full complexity can be daunting. It has been proposed that multidomain proteins have evolved a mechanism to minimize inter-domain interference. Also it has been proposed that domains can be treated as independent when the interfaces between them are small (Han et al., 2007). It was fortuitous that *Mm*Chi60, with its four domains linked in a chain, could be crystallized. The protein offered an opportunity to test the extent to which chain-like protein structures can be treated as assemblies of "Lego" blocks. Calorimetric studies of *Mm*Chi60 mutants show that its domains can fold independently, maintain their integrity and exhibit comparable heat stabilities when they are expressed in isolation, as when they are part of the protein. This could be related to the chain-like structure of *Mm*Chi60, with the domains having limited contact with each other. There are, however, indications of some interdomain dependence. Thus, treating flexibly connected domains as independent units can be successful, but shuffling the domains has limitations, as some combinations can undermine the protein's stability. This indicates that the stability of natural multidomain proteins is a result of evolutionary optimization to minimize destabilizing interference between the domains.

The CAT domain, with its evolutionarily ancient TIM-barrel fold—shared by approximately 10 % of known enzymes—is the most stable of the *Mm*Chi60 domains (Wierenga, 2001). Its melting profile, comprising at least two thermal transitions, may reflect an unfolding mechanism similar to that described for other TIM-barrel proteins, involving a

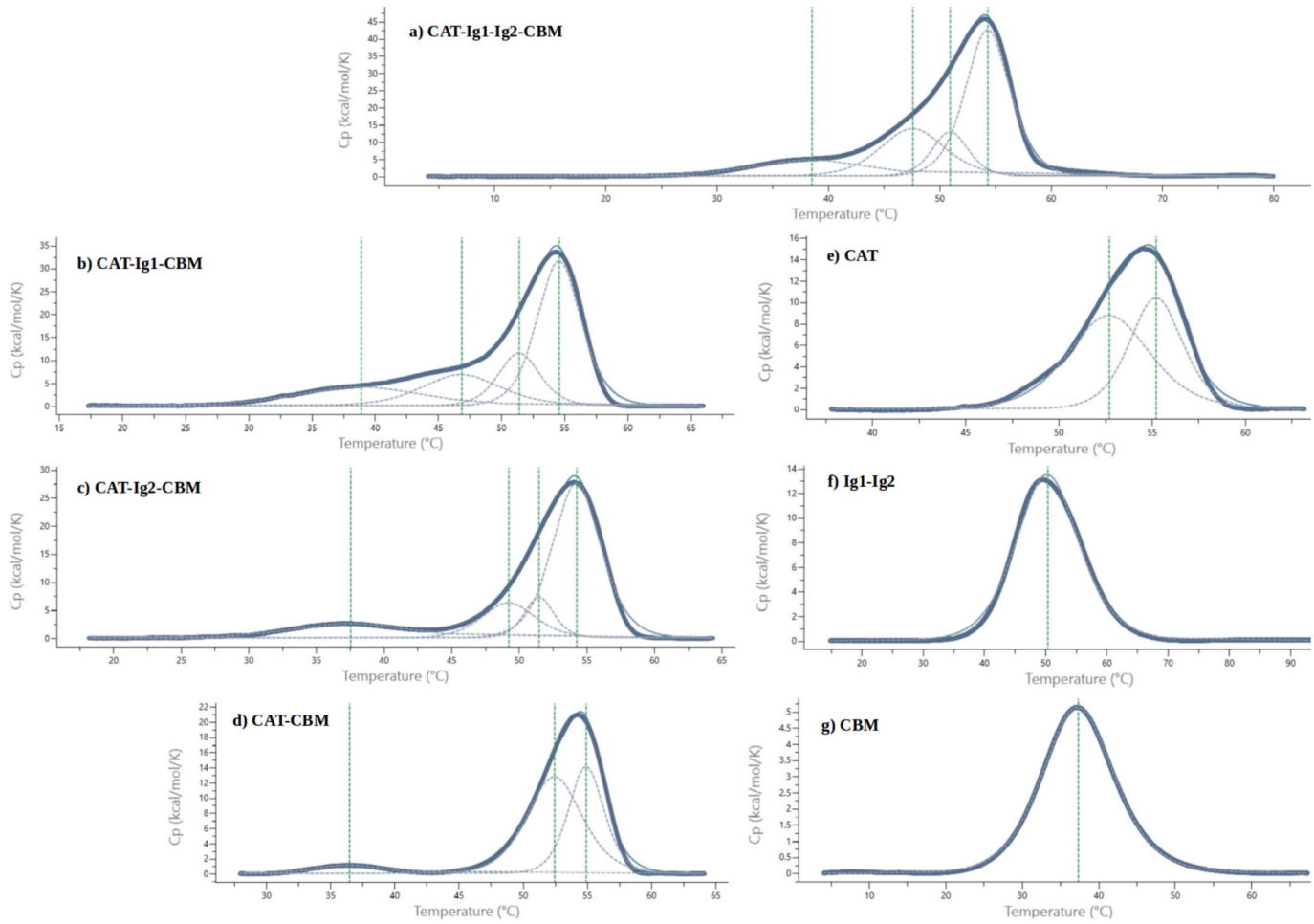

Fig. 8. Details of DSC melting curves of (**a**) native *Mm*Chi60 and (**b**-**g**) its deletion mutants. The solid line shows the overall melting profiles, while the dotted lines show the possible interpretations of the asymmetric experimental curves in terms of underlying Gaussian-like individual thermal events. The CAT domain is the most stable, with T_m of approximately 55 °C, while the CBM domain is the least stable, with T_m in the range 36–39 °C, depending on the construct. The Ig-like domains exhibit an intermediate stability, with T_m of 47–50 °C. Comparison of the curves shows that the domains maintain their structural integrity within the protein and in isolation, but they are also affected, to some extent, by the presence of other domains nearby. The meting profile of CAT is asymmetric, indicating that its unfolding is not a one-step process.

relatively stable central $(\beta\alpha)_4$ module flanked by less stable folding motifs (Gu et al., 2007). The CAT domain appears slightly more stable when isolated than when connected to other domains. Notably, it also produced the highest-quality crystals.

The CBM domain possesses well-defined structural features related to its function: three exposed Trp residues located on a flat protein surface and a flexible hinge that links it to the adjacent domain, allowing the CBM to swivel relative to the rest of the molecule. In the native *Mm*Chi60 structure, the three Trp side chains are solvent-exposed and co-planar. In the mutant structures, examined in this study, the Trp residues display flexibility as they interact with neighboring protein molecules (Fig. S4), and the hinge region on which the CBM pivots enables the domain to adopt diverse orientations relative to the remainder of the molecule.

The CBM is the least stable of the *Mm*Chi60 domains, though it remains sufficiently stable for the naturally cold environment of *Moritella marina*, which does not grow above 20 °C (Albright and Morita, 1972). The stability of CBM is slightly higher when it is attached to an Ig-like domain (as in the native protein and in the CAT–Ig1/Ig2–CBM mutants) than when it exists alone or is directly attached to the CAT domain. More importantly, it appears prone to degradation or cleavage when positioned adjacent to the CAT domain, as observed in the crystallization trials of the CAT–CBM mutants. This may suggest that the proximity of the large CAT domain destabilizes the smaller CBM domain.

Another example of an unstable combination of artificially joined domains is the CAT–Ig2–CBM mutant. Excision of the Ig1 domain and direct attachment of the CAT and Ig2 domains resulted in crystals consisting of only the CAT domain.

In contrast to the CAT and CBM domains, the function of the Ig-like domains in *Mm*Chi60 is less apparent. The Ig-like fold occurs in diverse proteins, often associated with cell adhesion or cell surface receptors, and is also found in many chitinases. These domains have been proposed to enhance molecular flexibility and increase the enzyme's effective radius as the chitinase explores the chitin surface around its attachment point, the CBM domain (Malecki et al., 2013). It has also been suggested that Ig-like domains contribute to the stabilization of multidomain proteins (Itoh et al., 2016). In the present case, the Ig-like domains may function as spacers between the CAT and CBM domains, which tend to undergo degradation when positioned directly adjacent to one another.

The temperature melting profile of the Ig1–Ig2 construct is nearly symmetric, with a maximum at 50 °C. The Ig-like domains appear slightly less stable when included in constructs containing CAT or CBM domains than when expressed independently. However, it should be noted that determining the melting temperature of the Ig-like domains in constructs that include the CAT domain may be uncertain due to overlapping thermal profiles.

Ig1 and Ig2 are likely the result of a genetic tandem repeat event.

Previous studies have raised the question of potential interdomain interference affecting the folding of tandem repeats (Han et al., 2007). It has been proposed that independent folding of domain can occur when interdomain interactions are limited. The Ig1–Ig2 tandem repeat, connected by a short interdomain linker, may exemplify this phenomenon. Moreover, it was also suggested that adjacent tandem domains may have diverged in amino acid sequence to prevent interdomain folding interference (Han et al., 2007). The Ig1 and Ig2 domains share 39 % amino acid sequence identity and 58 % similarity (Fig. S5), which appears to be sufficient to allow stable, independent folding.

The architecture of *Mm*Chi60 suggests that the enzyme is active as a monomer—flexibly attached to chitin at one end (*via* the CBM) while probing its surface with the CAT domain at the other end. The dimers observed in the crystal structure appear incompatible with such enzymatic activity, as the "plus" (aglycon) side of the substrate-binding surface is partially occluded between the interacting CAT domains. The 6a–6b β-hairpin, which is proposed to participate in chitin binding, is instead involved in CAT–CAT interactions.

Nevertheless, the persistence of the dimeric form in both the crystal structure of native *Mm*Chi60 and the CAT–Ig1–CBM mutant, suggests that the protein is capable of dimerization (Fig. 4). Preliminary cryo-EM results also indicate the presence of dimers of native *Mm*Chi60 (Fig. 6). Dimerization involves the CAT and Ig1 domains. In contrast, in the structures of CAT–CBM and CAT alone, the CAT domains interact differently, suggesting that the Ig1 domain is required for dimerization. This implies a role of the Ig1 domain in stabilizing the dimeric form of the free enzyme.

Earlier small-angle X-ray scattering (SAXS) studies reported that the scattering profile of *Mm*Chi60 in solution was not straightforward to interpret and was ultimately modeled as an ensemble of monomeric *Mm*Chi60 conformations (Malecki et al., 2014). However, it is possible that an alternative ensemble set, including dimers, could also fit the SAXS data. Dynamic light scattering (DLS) and gel filtration analyses were inconclusive due to the highly elongated shape of the *Mm*Chi60 molecule and provided no definitive insights into its oligomeric state.

It is plausible that *Mm*Chi60 exists in a dimeric form when not engaged with chitin. Dimerization could increase the stability of this long, flexible protein in solution (and may also have facilitated crystallization). Moreover, dimeric form of the free enzyme might enhance the enzyme's effectiveness in the sense that when a dimer encounters chitin, two enzyme molecules are immediately available to degrade it. On the other hand, the monomeric form of *Mm*Chi60, being more flexible, could enhance enzymatic activity by enabling more effective exploration of the chitin surface. The extended affinity for chitin (conferred by the CBM domain), flexibility (arising from the CBM's hinge connection to the rest of the protein), and long "reach" (provided by the Ig-like domains) appear to be structural adaptations that enhance the enzyme's effectiveness independent of the intrinsic catalytic efficiency of the active site.

4. Materials and methods

4.1. Gene manipulation and expression

The chitinase gene from the psychrophilic bacterium *Moritella marina* (*Mmchi60*), cloned into the pET11a plasmid (Novagen) and prepared as described by (Stefanidi and Vorgias, 2008), was kindly provided by Prof. Constantinos E. Vorgias (National and Kapodistrian University of Athens). In addition, the chitinase gene (excluding the 22-amino acid signal sequence) was cloned into the pET-151D-TOPO vector (Invitrogen) to introduce an N-terminal His-tag label removable by TEV protease during protein purification.

The above plasmids, containing the nucleotide sequence encoding all four *Mm*Chi60 domains (CAT, Ig1, Ig2, and CBM; Table 1), were amplified in *E. coli* DH5α, isolated using a Plasmid Miniprep DNA Purification Kit (EURx, Poland), and served as the source of genetic material for subsequent steps. Mutagenesis was performed using the PIPE (Polymerase Incomplete Primer Extension) method (Klock and Lesley, 2009). Several deletions mutants of *Mm*Chi60 were generated using Invitrogen Platinum SuperFi PCR Master Mix and specifically designed primers. The accuracy of the nucleotide sequences for all variants was verified by sequencing (Genomed S.A., Warsaw, Poland).

Subsequent chitinase mutants (derived from *Mm*Chi60 cloned into (i) pET11a and/or (ii) pET-151D-TOPO plasmids) included selected domain combinations: three mutants lacking one Ig-like domain (CAT–Ig1–CBM (i and ii), and CAT–Ig2–CBM (ii)); four mutants containing differently truncated CAT and CBM domains (CAT–CBM-5 (i and ii), CAT–CBM-8 (ii), CAT–CBM-2 (ii)); three single-domain mutants (CAT (i and ii), CBM (ii)); and one mutant containing both Ig-like domains (Ig1–Ig2 (ii)) (Table 1).

All the protein variants were expressed in BL21-Magic *E. coli* cells grown in LB medium supplemented with 100 μg/mL ampicillin and 25 μg/mL kanamycin. Expression was induced with 0.5 mM IPTG, followed by incubation for 16 h at 18 °C. The bacterial cells were then pelleted and stored at –80 °C for future use.

4.2. Protein purification and crystallization

Two different proteins purification protocols were used, depending on the plasmid type employed for expression: Protocol A for (i) pET11a plasmid-derived proteins, and Protocol B for (ii) pET-151D-TOPO plasmid-derived proteins.

Protocol A: The *Mm*Chi60 mutants expressed from the pET11a plasmid contained a 22-amino acid signal sequence at the N-terminus, which directed them to the periplasmic space. Osmotic shock, performed according to (Poole and Hancock, 1984), was used to selectively disrupt the outer cell membrane, thereby releasing only periplasmic contents. The cells were subsequently centrifuged at 10,000 rpm, and the supernatant was adjusted to 1 M ammonium sulfate and 20 mM sodium phosphate buffer (pH 8.0). The sample was then directly applied to a 10 mL Phenyl-Sepharose 6 Fast Flow column (GE Healthcare). The final purification step consisted of size-exclusion chromatography using a HiLoad 16/60 Superdex^{TM} 200 or 75 prep-grade column (GE Healthcare).

Protocol B: The mutants expressed from the pET-151D-TOPO plasmid were produced with an N-terminal His-tag. The cells were disrupted by sonication for 5–10 min at 10 °C in Standard Buffer (20 mM Tris HCl pH 8.0, 200 mM NaCl) supplemented with 10 % glycerol, 1 % Triton X-100, and 20 mM imidazole. Soluble and insoluble protein fractions were separated by centrifugation (20,000 rpm, 30 min, 10 °C). The purification process consisted of the following steps: (i) His-trap affinity chromatography using a High Performance Sepharose column (GE Healthcare); (ii) dialysis combined with TEV protease digestion (the protease carried a permanent His-tag); (iii) a second His-trap affinity chromatography step to remove undigested protein, the protease, and His-tag debris; and (iv) size-exclusion chromatography using a HiLoad 16/60 Superdex^{TM} 200 or 75 prep-grade column (GE Healthcare).

All purification steps were monitored by SDS–PAGE. After purification, protein samples were dialyzed against Standard Buffer and concentrated to 7.7–12.0 mg/mL using Amicon® Ultra centrifugal filters (Merck Millipore Ltd.). Crystallization screening was performed using the sitting drop vapor diffusion method at 18 °C, with a Gryphon crystallization robot (Art Robbins Instruments) and commercial crystallization kits. Subsequent optimization of crystallization conditions was conducted using the hanging drop vapor diffusion method.

Crystals of CAT–Ig1–CBM were grown in 0.1 M MES/imidazole buffer (pH 6.5) containing 10 % (*w/v*) PEG 20000 and 20 % (*w/v*) PEG MME 550, supplemented with a monosaccharide mix (20 mM each of D-glucose, D-mannose, D-galactose, L-fucose, and D-xylose) and 1mM *N*-acetyl-D-glucosamine (GlcNAc). The CAT–CBM-5 mutant was crystallized under several conditions, but only one (0.1 M HEPES (pH 7.0), 1.1 M sodium malonate, and 0.5 % Jeffamine ED-2001) produced crystals

containing both expected domains (PDB ID 9FBP). All other CAT–CBM-5 crystallizations yielded crystals containing only the CAT domain, obtained under the following conditions: (i) 0.1 M Bis-Tris (pH 5.5), 45 % (*v/v*) MPD, 0.2 M ammonium acetate (PDB ID: 4W5Z); (ii) 0.1 M HEPES (pH 7.5), 22 % (*w/v*) PAA, 0.02 M $MgCl_2$, and 2 mM $(GlcNAc)_4$ (PDB ID: 9FBR); (iii) 0.1 M Tris (pH 8.0), 20 % (*w/v*) PEG 4000, and 0.4 M $MgCl_2$ (PDB ID: 9FBS). The isolated CAT protein crystallized in 3.4 M sodium malonate (pH 6.0) (PDB ID: 9FBQ).

4.3. X-ray data collection, structure solution and model refinement

X-ray diffraction data were collected on synchrotron beamlines P13, operated by EMBL Hamburg at the PETRA III storage ring (DESY, Hamburg, Germany) (Cianci et al., 2017), and 14.1 and 14.2 at the BESSY II storage ring operated by Helmholtz-Zentrum Berlin (Mueller et al., 2015). Prior to freezing, crystals were immersed in cryoprotecting solution prepared by mixing the reservoir solution with glycerol or PEG 400 to achieve a cryoprotectant concentration of 25–30 % (*v/v*) or were flash-frozen directly without the addition of cryoprotectant.

Diffraction data were processed using the XDS program (Kabsch, 2010), and data collection statistics are summarized in Table 2. The structures were solved using Phaser (McCoy et al., 2007) from the CCP4 program suite (Winn et al., 2011), employing suitable fragments of the full-length *Mm*Chi60 structure as search models. An exception was the structure containing the CAT and CBM domains (PDB ID: 9FBP) in which the CBM domain was fitted manually in the difference electron density. Molecular models were built and adjusted using Coot (Emsley et al., 2010) and refined with Refmac5 (Murshudov et al., 2011) or Phenix (Afonine et al., 2012). Ion assignments for both Na^+ and Cl^- were done based on the strength of the electron density peaks, analysis of the local electrostatic environment and the coordination geometry together with the characteristic bond lengths.

4.4. Cryo-EM sample preparation, data collection and processing

Preparation of the cryo-EM samples and data collection were carried out at the SOLARIS Cryo-EM Facility (Kraków, Poland). Quantifoil TEM grids (300 mesh R2/1 copper) were glow-discharged using a Leica EM ACE200 (Leica Microsystems) discharger. A 3.0 µL aliquot of the *Mm*Chi60 sample at a concentration of 0.3 mg/mL was applied to the grid and plunge-frozen in liquid ethane using an FEI Vitrobot Mark IV. The device was operated at 100 % humidity and 4 °C, with the following blotting parameters: blot time of 4 s, wait time of 10 s, and blot force set to 0.

A total of 6174 cryo-EM micrographs were collected at the SOLARIS National Cryo-EM Centre (Kraków, Poland). Data acquisition was performed on a Thermo Fisher Scientific Titan Krios G3i microscope operating at 300 kV. The imaging system consisted of a Gatan K3 direct electron detector operating in counting mode and a Gatan BioQuantum energy filter (20 eV slit width). Data were collected at a nominal magnification of 105,000×, corresponding to a physical pixel size of 0.85 Å. Each movie comprised 40 frames, with a total accumulated electron dose of 40.57$e^-/Å^2$ across a defocus range of −0.9 to −3.0 µm.

Cryo-EM data processing was conducted in CryoSPARC v4.1 (Punjani et al., 2017). Raw movie stacks were imported and subjected to patch-based motion correction using the *Patch Motion Correction* job. The contrast transfer function (CTF) parameters for each motion-corrected micrograph were estimated using the Patch CTF Estimation job. Micrographs exibiting poor quality were discarded, resulting in a final dataset of 5917 micrographs for downstream analysis.

An initial set of 1,864,008 particles was automatically picked using the *Blob Picker* and extracted with a box size of 340 pixels. This particle set was subjected to multiple rounds of 2D classification to remove contaminants and poorly defined particles. The resulting 2D class averages clearly indicated a predominant dimeric architecture for the protein, with a minor fractions corresponding to monomeric species. However, subsequent attempts to generate a stable *ab initio* 3D model

Table 2
Summary of X-ray data and model refinement.

Domains present in the crystal structure	CAT-Ig1-CBM	CAT-CBM	CAT	CAT	CAT	CAT
PDB ID	9FBO	9FBP	4W5Z	9FBQ	9FBR	9FBS
Space group	R3	$P2_1$	$C222_1$	$C222_1$	$C222_1$	$C222_1$
Unit cell parameters						
a (Å)	225.74	44.79	50.69	51.11	50.50	50.76
b (Å)	225.74	172.83	72.69	72.59	74.09	74.01
c (Å)	65.31	47.09	171.17	174.9	175.57	172.54
α (°)	90	90	90	90	90	90
β (°)	90	90.01	90	90	90	90
γ (°)	120	90	90	90	90	90
Wavelength (Å)	0.9763	0.9171	0.9763	0.9184	0.9168	0.9184
Beamline	EMBL P13	BESSY 14.1	BESSY 14.2	BESSY 14.2	BESSY 14.1	BESSY 14.1
Temperature (K)	100	100	100	100	100	100
Resolution (Å)	2.69	1.84	1.32	1.48	1.74	2.35
R_{merge} [#]	0.09 (0.86)*	0.061 (0.437)	0.054 (1.04)	0.080 (0.81)	0.085 (0.85)	0.144 (0.96)
Completeness (%)	98.4 (93.2)	88.8 (78.1)	99.1 (95.8)	99.6 (98.0)	97.4 (97.1)	99.3 (96.0)
No. of reflections	33 937	53 484	74 674	54 649	32 174	13 787
<I/σ(I)>	14.1 (1.5)	10 (1.6)	17 (1.7)	14.1 (2.1)	10.0 (1.3)	12.7 (2.2)
Protein subunits / asymmetric unit	2	2	1	1	1	1
R[§] / R_{free}[$]	0.194/0.252	0.155/0.219	0.111/ 0.150	0.176/0.209	0.178/0.222	0.186/0.266
Raw diffraction images DOI	https://doi.org/10.60884/HHYBFS	https://doi.org/10.60884/5EAP06	n.a.	https://doi.org/10.60884/QEGI6Y	https://doi.org/10.60884/ZQ45LG	https://doi.org/10.60884/M7LARR

*Values in brackets are for the highest resolution shell.

[#] $R_{merge} = \Sigma_{hkl}\Sigma_i|I_i(hkl) - <I(hkl)>|/\Sigma_{hkl}\Sigma_i I_i(hkl)$, where $I_i(hkl)$ is the integrated intensity of a given reflection and $< I(hkl) >$ is the mean intensity of multiple corresponding symmetry-related reflections.

[§] $R = \Sigma_{hkl}||F_{obs}| - |F_{calc}||/\Sigma_{hkl}|F_{obs}|$, where F_{obs} and F_{calc} are the observed and calculated structure factors, respectively.

[$] R_{free} is R calculated using a randomly chosen subset of reflections excluded from the refinement.

from the curated particle stack were unsuccessful, preventing further 3D refinement.

4.5. Differential scanning calorimetry

The thermal stability of *Mm*Chi60 variants was analyzed using a MICROCAL PEAQ-DSC system (Malvern Instruments Ltd). Each DSC experiment comprised stages conducted under identical conditions: (i) five reference scans with buffer-filled cells to establish the instrument's thermal history and ensure baseline reproducibility, and (ii) one sample-buffer scan to acquire the experimental data for analysis.

Prior to each DSC experiment, the protein samples were dialyzed against Storage Buffer (20 mM HEPES, pH 7.5, 200 mM NaCl), which was subsequently used in the DSC measurements. Protein concentration, determined using a NanoDrop spectrophotometer, ranged from 20 to 600 μM. Experimental parameters included a temperature range of 2–130 °C, a scan rate of 60 °C/h, and operated in medium feedback mode. The data were analyzed using the dedicated software provided by Malvern Instruments.

CRediT authorship contribution statement

Magdalena Bejger: Writing – original draft, Visualization, Validation, Investigation, Conceptualization. **Piotr H. Małecki:** Validation, Investigation, Data curation, Conceptualization. **Katarzyna Biniek-Antosiak:** Investigation. **Wojciech Rypniewski:** Writing – original draft, Validation, Supervision, Project administration, Funding acquisition, Data curation, Conceptualization.

Declaration of competing interest

The authors declare that they have no known competing financial interests or personal relationships that could have appeared to influence the work reported in this paper.

Acknowledgments

The research was co-funded by the National Science Centre, Poland (UMO-2017/27/B/NZ1/02201). We gratefully acknowledge Polish high-performance computing infrastructure PLGrid (HPC Center: ACK Cyfronet AGH) for providing computer facilities and support within computational grant no. PLG/2024/017216. Research at the National Synchrotron Radiation Centre SOLARIS is supported by the Ministry of Science and Higher Education, Poland, under contract no. 1/SOL/2021/2. The authors thank Future Synthesis sp. z o.o. for support and reagents and Translmed Publishing Group for language editing.

Appendix A. Supplementary data

Supplementary data to this article can be found online at https://doi.org/10.1016/j.jsb.2025.108282.

Data availability

The refined atomic coordinates of the *Mm*Chi60 deletion mutants were deposited in the Protein Data Bank (PDB) under the IDs listed in Table 2. The raw X-ray diffraction images were deposited in the Macrocrystallographic Xtal-lography Raw Data Repository (MX-RDR) and are available under the DOI addresses given in Table 2.

References

Afonine, P.V., Grosse-Kunstleve, R.W., Echols, N., Headd, J.J., Moriarty, N.W., Mustyakimov, M., Terwilliger, T.C., Urzhumtsev, A., Zwart, P.H., Adams, P.D., 2012. Towards automated crystallographic structure refinement with phenix.refine. Acta Cryst D 68, 352–367. https://doi.org/10.1107/S0907444912001308.

Albright, L.J., Morita, R.Y., 1972. Effects of environmental parameters of low temperature and hydrostatic pressure on L-serine deamination byVibrio marinus. J. Oceanogr. Soc. Jpn. 28, 63–70. https://doi.org/10.1007/BF02109721.

Barclay, A.N., 1999. Ig-like domains: Evolution from simple interaction molecules to sophisticated antigen recognition. PNAS 96, 14672–14674. https://doi.org/10.1073/pnas.96.26.14672.

Cianci, M., Bourenkov, G., Pompidor, G., Karpics, I., Kallio, J., Bento, I., Roessle, M., Cipriani, F., Fiedler, S., Schneider, T.R., 2017. IUCr, P13, the EMBL macromolecular crystallography beamline at the low-emittance PETRA III ring for high- and low-energy phasing with variable beam focusing. urn:issn:1600–5775 24, 323–332. https://doi.org/10.1107/S1600577516016465.

Davies, G.J., Wilson, K.S., Henrissat, B., 1997. Nomenclature for sugar-binding subsites in glycosyl hydrolases. Biochem. J 321, 557–559. https://doi.org/10.1042/bj3210557.

Emsley, P., Lohkamp, B., Scott, W.G., Cowtan, K., 2010. Features and development of Coot. Acta Crystallogr. Section D, Biol. Crystallogr. 66, 486–501. https://doi.org/10.1107/S0907444910007493.

Gu, Z., Rao, M.K., Forsyth, W.R., Finke, J.M., Matthews, C.R., 2007. Structural analysis of kinetic folding intermediates for a TIM barrel protein, indole-3-glycerol phosphate synthase, by hydrogen exchange mass spectrometry and Gō-model simulation. J. Mol. Biol. 374, 528–546. https://doi.org/10.1016/j.jmb.2007.09.024.

Han, J.-H., Batey, S., Nickson, A.A., Teichmann, S.A., Clarke, J., 2007. The folding and evolution of multidomain proteins. Nat. Rev. Mol. Cell Biol. 8, 319–330. https://doi.org/10.1038/nrm2144.

Ikegami, T., Okada, T., Hashimoto, M., Seino, S., Watanabe, T., Shirakawa, M., 2000. Solution structure of the chitin-binding domain of *Bacillus circulans* WL-12 chitinase A1*. J. Biol. Chem. 275, 13654–13661. https://doi.org/10.1074/jbc.275.18.13654.

Itoh, T., Hibi, T., Suzuki, F., Sugimoto, I., Fujiwara, A., Inaka, K., Tanaka, H., Ohta, K., Fujii, Y., Taketo, A., Kimoto, H., 2016. Crystal structure of chitinase ChiW from Paenibacillus sp. str. FPU-7 reveals a novel type of bacterial cell-surface-expressed multi-modular enzyme machinery. PLoS One 11, e0167310. https://doi.org/10.1371/journal.pone.0167310.

Kabsch, W., 2010. XDS. Acta Crystallographica Section D: Biological Crystallography 66, 125. Doi: 10.1107/S0907444909047337.

Klock, H.E., Lesley, S.A., 2009. The Polymerase Incomplete Primer Extension (PIPE) method applied to high-throughput cloning and site-directed mutagenesis. Methods Mol. Biol. 498, 91–103. https://doi.org/10.1007/978-1-59745-196-3_6.

Lin, F.-P., Wu, C.-Y., Chen, H.-N., Lin, H.-J., 2015. Effects of C-terminal domain truncation on enzyme properties of Serratia marcescens chitinase C. Appl. Biochem. Biotechnol. 175, 3617–3627. https://doi.org/10.1007/s12010-015-1530-5.

Liu, J., Xu, Q., Wu, Y., Sun, D., Zhu, J., Liu, C., Liu, W., 2023. Carbohydrate-binding modules of ChiB and ChiC promote the chitinolytic system of *Serratia marcescens* BWL1001. Enzyme Microb. Technol. 162, 110118. https://doi.org/10.1016/j.enzmictec.2022.110118.

Malecki, P.H., Raczynska, J.E., Vorgias, C.E., Rypniewski, W., 2013. Structure of a complete four-domain chitinase from Moritella marina, a marine psychrophilic bacterium. Acta Cryst. D 69, 821–829. https://doi.org/10.1107/S0907444913002011.

Malecki, P.H., Vorgias, C.E., Petoukhov, M.V., Svergun, D.I., Rypniewski, W., 2014. Crystal structures of substrate-bound chitinase from the psychrophilic bacterium Moritella marina and its structure in solution. Acta Cryst. D 70, 676–684. https://doi.org/10.1107/S1399004713032264.

McCoy, A.J., Grosse-Kunstleve, R.W., Adams, P.D., Winn, M.D., Storoni, L.C., Read, R.J., 2007. Phaser crystallographic software. J. Appl. Cryst. 40, 658–674. https://doi.org/10.1107/S0021889807021206.

Mueller, U., Förster, R., Hellmig, M., Huschmann, F.U., Kastner, A., Malecki, P., Pühringer, S., Röwer, M., Sparta, K., Steffien, M., Ühlein, M., Wilk, P., Weiss, M.S., 2015. The macromolecular crystallography beamlines at BESSY II of the Helmholtz-Zentrum Berlin: Current status and perspectives. Eur. Phys. J. Plus 2015 130:7 130, 1–10. Doi: 10.1140/EPJP/I2015-15141-2.

Murshudov, G.N., Skubák, P., Lebedev, A.A., Pannu, N.S., Steiner, R.A., Nicholls, R.A., Winn, M.D., Long, F., Vagin, A.A., 2011. REFMAC5 for the refinement of macromolecular crystal structures. Acta Crystallogr. D Biol. Crystallogr. 67, 355. https://doi.org/10.1107/S0907444911001314.

Poole, K., Hancock, R.E.W., 1984. Phosphate transport in Pseudomonas aeruginosa. Eur. J. Biochem. 144, 607–612. https://doi.org/10.1111/j.1432-1033.1984.tb08508.x.

Punjani, A., Rubinstein, J.L., Fleet, D.J., Brubaker, M.A., 2017. cryoSPARC: algorithms for rapid unsupervised cryo-EM structure determination. Nat. Methods 14, 290–296. https://doi.org/10.1038/nmeth.4169.

Stavros, P., Malecki, P.H., Theodoridou, M., Rypniewski, W., Vorgias, C.E., Nounesis, G., 2015. The stability of the TIM-barrel domain of a psychrophilic chitinase. Biochem. Biophys. Rep. 3. https://doi.org/10.1016/j.bbrep.2015.07.016.

Stefanidi, E., Vorgias, C.E., 2008. Molecular analysis of the gene encoding a new chitinase from the marine psychrophilic bacterium Moritella marina and

biochemical characterization of the recombinant enzyme. Extremophiles 12, 541–552. https://doi.org/10.1007/s00792-008-0155-9.

Wang, W., Ma, T., Zhang, B., Yao, N., Li, M., Cui, L., Li, G., Ma, Z., Cheng, J., 2014. A novel mechanism of protein thermostability: a unique N-terminal domain confers heat resistance to Fe/Mn-SODs. Sci. Rep. 4, 7284. https://doi.org/10.1038/srep07284.

Wierenga, R.K., 2001. The TIM-barrel fold: a versatile framework for efficient enzymes. FEBS Lett. 492, 193–198. https://doi.org/10.1016/S0014-5793(01)02236-0.

Winn, M.D., Ballard, C.C., Cowtan, K.D., Dodson, E.J., Emsley, P., Evans, P.R., Keegan, R. M., Krissinel, E.B., Leslie, A.G.W., McCoy, A., McNicholas, S.J., Murshudov, G.N., Pannu, N.S., Potterton, E.A., Powell, H.R., Read, R.J., Vagin, A., Wilson, K.S., 2011. Overview of the CCP4 suite and current developments. Acta Crystallogr. Section D, Biol. Crystallogr. 67, 235–242. https://doi.org/10.1107/S0907444910045749.